



Laurent MAGRI-STELLA

Cosmic Bananas: Measuring weak gravitational flexion in Horizon-AGN hydrodynamical cosmological simulation

MASTER'S THESIS
to achieve the university degree of
Fundamental Physics National Master Diploma

submitted to
Aix-Marseille Université

Supervised by
Raphaël GAVAZZI
Chargé de Recherche, CNRS
Laboratoire d'Astrophysique de Marseille
LAM (UMR7326)

Marseille, March - July 2024

Every model is wrong, but some are useful – George E.P. Box

Contents

1	Introduction	1
1.1	Motivation	1
1.2	Research Questions and Contributions	2
1.3	Thesis Structure and Organisation	2
2	Theory and formalism of weak gravitational lensing	4
2.1	A quick historical review of the first derivations and proofs of gravitational lensing	4
2.2	The bases of gravitational lensing	5
3	Simulation, data and methods	8
3.1	The Horizon-AGN simulation	8
3.2	Data definition and analysis	9
3.3	Mass density profiles	13
3.3.1	The Singular Isothermal Sphere (SIS) model	13
3.3.2	The Navarro-Frenk-White (NFW) model	14
3.4	Numerical lensing measurement	16
4	Results and interpretation	19
4.1	Tools and discussion	19
4.1.1	Julia	19
4.1.2	Error estimation	19
4.2	Thin lens planes and lensing maps	20
4.3	Numerical correlation computation and results	22
4.4	The difference between satellite and central galaxies	24
4.5	Fitting the SIS and NFW models	26
4.5.1	Central galaxies	26
4.5.2	Satellite galaxies	27
5	Euclid, SourceExtractor++ and Machine Learning	28
5.1	The Euclid Survey	28
5.2	SourceExtractor++	28
5.3	ONNX	29
6	Conclusion and Future Work	30
Bibliography		31

Contents

7 Appendix	32
A Julia code for computing the lensing maps	32
B Julia code for computing the galaxy-galaxy lensing correlation function	37
List of Figures	41
List of Tables	42
List of Listings	43

CHAPTER 1

Introduction

In our vast Universe, where galaxies twinkle and space-time bends, gravitational lensing emerges as a compelling artifact predicted by the theory of General Relativity, even if it was also inscribed in Newtonian theory. It is now regarded as one of the best cosmological probes, providing insight into the intricate interaction between the nature of matter and gravity on cosmic scales. Among its various manifestations, weak gravitational flexion stands out as a promising avenue for exploration, holding the potential to elucidate the nature of dark matter. This Master thesis stands as a short investigation into weak gravitational flexion, with the goal of refining our understanding and leveraging it to constrain dark matter models.



While gravitational lensing has a rich historical context, with significant attention traditionally directed towards shear, the exploration of flexion is an interesting deepening of this domain. Our research builds upon existing knowledge, seeking not to introduce novel concepts but rather to delve deeper into established frameworks. By extending our analysis from shear to flexion, our aim is to extract additional information regarding the distribution of matter in the universe, particularly concerning its implications for dark matter.

1.1 Motivation

The Euclid satellite, led by the European Space Agency (ESA), aims to map the geometry of the dark universe by observing an unprecedented amount of galaxies over a third of the sky. Its primary goal is to investigate dark energy and dark matter, which make up about 95% of the universe's mass-energy content. Equipped with a visible imaging channel (VIS) and a near-infrared spectrometer and photometer (NISP), Euclid will measure the shapes and redshifts of distant galaxies with a precision never achieved before. This will provide crucial data for understanding the universe's expansion history and the growth of cosmic structures.

Gravitational lensing, including shear, convergence, and especially flexion which is the main focus of this work, is essential for Euclid's mission.

- **Shear** measures the distortion of galaxy shapes due to gravitational fields, providing insights into the distribution of dark matter.
- **Convergence** refers to the magnification of light from distant objects, helping to map mass distribution, including dark matter halos.
- **Flexion** captures higher-order distortions, offering more detailed information about the gravitational field and substructures within dark matter halos.

By analyzing these lensing effects, Euclid will test theories of gravity on cosmic scales and enhance our understanding of the universe's fundamental properties.

Our exploration is guided by the overarching objective of constraining dark matter models, using insights obtained from weak gravitational flexion to refine our comprehension of this matter constituent. By observing this phenomenon, in simulated data as well as images from space satellites, we hope to gain insights into the distribution and properties of dark matter, thereby advancing our pursuit to unravel its mysteries.

To achieve these objectives, we adopt an interdisciplinary approach, selecting and using tools and techniques from theoretical physics, computational modeling, and observational cosmology. Through the integration of numerical simulations, statistical analyses, and observational data, we aim to build an efficient and complete study of the data provided.

1.2 Research Questions and Contributions

The primary questions we aim to understand in this work are the following :

- What insights can weak gravitational flexion offer into the distribution and properties of dark matter on cosmic scales?
- What empirical results can be obtained to validate the compatibility of current models with observational reality?
- To what extent can we expect the incorporation of flexion to enhance our results, precision and interpretations from what we could do before using only shear?

1.3 Thesis Structure and Organisation

We will start by going through the theoretical grounds needed to work through gravitational lensing and how does one express the different terms in the Jacobian to highlight what we need to measure, and how we will do so. We will present the Horizon-AGN hydrodynamical cosmological simulation, which cosmology it uses, as well as the numerical methods it uses to generate a volume of Universe. We will describe the way we used Horizon-AGN to generate some data to work on, explaining the nature of this data in the mean time. We will then go on to present the methodology of our analysis, the tools and methods used and finally present and interpret the results. We will also include a short section on how the internship work will

end, as it carries on for a bit after the report deadline, explaining how we intend to adapt this whole analysis to Euclid by using Machine Learning tools to modify the well known and used software SourceExtractor to include the flexion components to its parameter fitting list.

CHAPTER 2

Theory and formalism of weak gravitational lensing

2.1 A quick historical review of the first derivations and proofs of gravitational lensing

Quite notably for gravitational lensing, theory came first and then the observational proofs followed, which is unusual for astronomical research, where observation is usually the first step to understand a physical phenomenon.

Gravitational lensing, funnily enough, can be treated under a Newtonian point of view, considering the movement of a light corpuscle (which is a theory supported by Newton himself) along a hyperbolic trajectory of a test particle, travelling at the speed of light under the action of Newtonian gravity. Note that under those assumptions, we are not talking about photons, as those are only defined in relativistic field theories, but about *light corpuscles* moving at a speed $v = c$. Considering a point mass of mass M responsible for the force felt by a mass m test particle,

$$\vec{F} = -\frac{GMm}{r^2}\hat{r} \quad (2.1)$$

one can write the velocity boost felt by the corpuscle as

$$\Delta\vec{v} = -\int_0^t d\tau \frac{GM}{r(\tau)^2}\hat{r}(\tau) \quad (2.2)$$

which, as in thoroughly developed in [1], once worked out, considering a constant speed of light on the parallel direction of travel and that the deflection of light is small, gives the following result for the angle of deflection of the light corpuscle,

$$\Psi_N = \frac{2GM}{c^2 r} \quad (2.3)$$

which is half the result predicted by Einstein's theory of General Relativity

$$\Psi_{GR} = \frac{4GM}{c^2 r} \quad (2.4)$$

The Newtonian result was supposed by Newton in 1704 and predicted by Henry Cavendish and Johann Georg von Soldner between 1784 and 1804, while the GR prediction of the value was computed by Einstein in 1911, while completing his theory of relativity. The first observation of the bending of the path of light was made by Eddington and Dyson in 1919 during a solar eclipse, which allowed for stars near the Sun to be seen. Those observations showed that the positions of those stars was slightly out of place, proving that the light was being lensed by the Sun.

From this point, gravitational lensing was a bit forgotten and thought of as a "fun" artifact from general relativity, studied and theorized by many physicists as Zwicky or Klimov. Then came the 80s, when astronomers understood that using CCD imaging, they could measure data from millions of stars and observe so-called *microlensing* events.

2.2 The bases of gravitational lensing

Whenever a physicist thinks of lenses, they might get reminded of geometrical optics classes, as such, gravitational lensing also has its own lens equation.

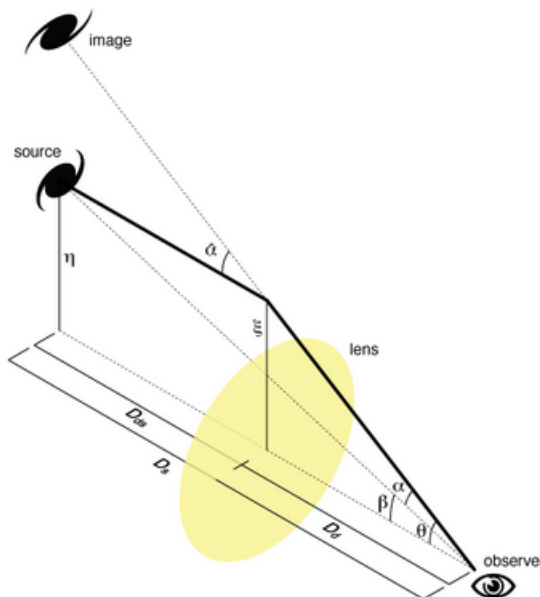


Figure 2.1: Definition of lensing angles and distances. Figure by Michael SACHS

Using 2.1, we can write the following equation, which is just a difference of angles, up to a factor of distances ratio, called the *lens equation*,

$$\vec{\beta} = \vec{\theta} - \frac{D_{ds}}{D_s} \hat{\alpha}(D_d \vec{\theta}) \quad (2.5)$$

we can use (2.5) to write the Jacobian of the coordinate transformation between image and

source plans, or respectively, lensed and unlensed plans,

$$\frac{\partial \beta_i}{\partial \theta_j} = \delta_{ij} - \frac{\partial \alpha_i}{\partial \theta_j} = A_{ij} \quad (2.6)$$

we can then decompose this matrix as a diagonal term and a trace-free term, which will contain important quantities for the rest of the work, respectively the scalar convergence κ and the 2-spinor shear γ

$$A = \begin{pmatrix} 1 - \kappa & 0 \\ 0 & 1 - \kappa \end{pmatrix} - \gamma \begin{pmatrix} \cos(2\phi) & \sin(2\phi) \\ \sin(2\phi) & -\cos(2\phi) \end{pmatrix} \quad (2.7)$$

where ϕ is the angle between $\vec{\alpha}$ and the x-axis (???) The convergence is responsible for increasing the size of the lensed object, the image, and conserving its surface brightness, therefore *magnifying* the object and increasing its appearing luminosity. The shear on the other hand causes more geometrical consequences on the image, it stretches it tangentially, meaning it seems to align on the gradient of the lensing potential.

Before diving further into how we accurately measure those quantities, let us define two new lensing fields that will be the core of the work of this report.

As you might have seen, eq.(2.7) is only an approximation to the first order of the matrix A_{ij} defined in eq.(2.6). But since convergence and shear are not constant within a galaxy image, we need to go to the next order to have a more precise description of the coordinate transformation, i.e. to the second order in deflection angle derivatives, or equivalently, third order in lensing potential derivatives,

$$A_{ij} = \frac{\partial \beta_i}{\partial \theta_j} = \delta_{ij} - \frac{\partial \alpha_i}{\partial \theta_j} - \frac{\partial^2 \alpha_i}{\partial \theta_j \partial \theta_k} d\theta_k = \delta_{ij} - \frac{\partial^2 \psi_i}{\partial \theta_j \partial \theta_k} d\theta_k - \frac{\partial^3 \psi_i}{\partial \theta_j \partial \theta_k \partial \theta_l} d\theta_k d\theta_l \quad (2.8)$$

As in [2], we can use a complex representation of our fields and a complex gradient operator,

$$\partial = \partial_1 + i\partial_2 \quad (2.9)$$

to express conveniently all of our lensing quantities, this also allows us to generate and thus reexpress our fields in a new manner. Thus, the displacement field α becomes

$$\alpha = \partial \psi = \alpha_1 + i\alpha_2 \quad (2.10)$$

applying this operator (which increases the field's spin by 1) and its conjugate ∂^* , (which lowers the spin by 1) on the lensing potential successively generates new expressions for κ and γ and the new lensing quantities we will be interested in. Thus, the spin-0 convergence field becomes

$$\kappa = \frac{1}{2} \partial^* \partial \psi = \frac{1}{2} \partial^* \alpha \quad (2.11)$$

and the spin-2 shear field,

$$\gamma = \frac{1}{2} \partial \partial \psi = \frac{1}{2} \partial \alpha = \gamma_1 + i\gamma_2 \quad (2.12)$$

We can now express in a simple way the third derivatives of the lensing potential with this formalism, giving us new fields \mathcal{F} and \mathcal{G}

$$\mathcal{F} = \partial \kappa = \frac{1}{2} \partial \partial^* \partial \psi = |\mathcal{F}| e^{i\phi} \quad (2.13)$$

$$\mathcal{G} = \partial \gamma = \frac{1}{2} \partial \partial \partial \psi = |\mathcal{G}| e^{3i\phi} \quad (2.14)$$

using that $\partial \kappa = \partial^* \gamma$ because ∂ commutes with its conjugate, eq.(??) and eq.(2.9), we can express in an exploitable way the two new lensing fields \mathcal{F} and \mathcal{G} , called respectively 1-flexion or first flexion, and 3-flexion or second flexion.

$$\mathcal{F} = \partial_1 \gamma_1 + \partial_2 \gamma_2 + i(\partial_1 \gamma_2 - \partial_2 \gamma_1) = \mathcal{F}_1 + i\mathcal{F}_2 \quad (2.15)$$

$$\mathcal{G} = \partial_1 \gamma_1 - \partial_2 \gamma_2 + i(\partial_1 \gamma_2 + \partial_2 \gamma_1) = \mathcal{G}_1 + i\mathcal{G}_2 \quad (2.16)$$

as a result, we are left with a total of 7 independant lensing fields, all expressed from various derivative combinations of the deflection angle α , namely $\kappa, \gamma_1, \gamma_2, \mathcal{F}_1, \mathcal{F}_2, \mathcal{G}_1$ and \mathcal{G}_2 . Those 4 new quantities called flexion terms account for the deformation and "arc-ed" aspect that can happen when observing gravitational lenses. Studying the behaviour of those fields should allow us to better understand the link between *weak* and *strong* gravitational lensing.

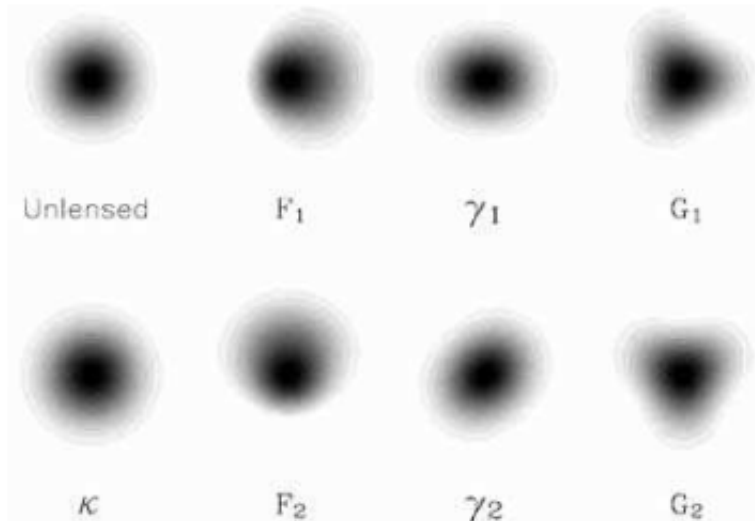


Figure 2.2: Effects of the different lensing fields on a Gaussian galaxy of radius 1 arcsec. 10% convergence/shear and 0.28 arcsec $^{-1}$ flexion (which is a very large value for this quantity, chosen only for visualizing) are applied. Figure extracted from [2]

We will focus our analysis on those 7 quantities, but one could obviously go higher in orders of derivatives, the next order would be composed of 3 fields of spin 4,2 and 0, and the next of 3 fields of spin 5,3 and 1 and so on.

CHAPTER 3

Simulation, data and methods

3.1 The Horizon-AGN simulation

The Horizon-AGN simulation is a hydrodynamical simulation of a volume of the universe. This simulation, which offers many possibilities to study cosmological and astrophysical phenomena, presented, for instance, in [3], uses the RAMSES code from [4], a N-body method designed to study structure formation across the Universe, it uses AMR (adaptive mesh refinement) to simulate, in [3] for example, up to 1024^3 dark matter particles in a square box of side $100 h^{-1}$ Mpc. The mass resolution is thus $8 \cdot 10^7 h^{-1} M_\odot$. The chosen cosmology is a standard flat Λ CDM, and its parameters are listed in the following table.

H_0	Ω_b	Ω_{dm}	Ω_Λ	σ_8	n_s
70.4	0.045	0.227	0.728	0.81	0.967

Table 3.1: List of parameters used for the flat Λ CDM cosmology defined in the Horizon-AGN simulation and their values, all parameters are unitless, except for the Hubble parameter H_0 , expressed in $\text{km s}^{-1}\text{Mpc}^{-1}$

In this simulation, the gas evolution is computed with a second-order unsplit Godunov scheme for the Euler equation. The interpolated variables are reconstructed using the Harten-Lax-van Leer-Contact Riemann solver (presented in [5]). The gas is heated via a uniform UV background that originated from the reionization epoch at $z = 10$, while its cooling is allowed via H and He collisions. Schmidt law is used to model star formation, and black hole formation occurs when the gas density reaches 0.1 H.cm^{-3} .

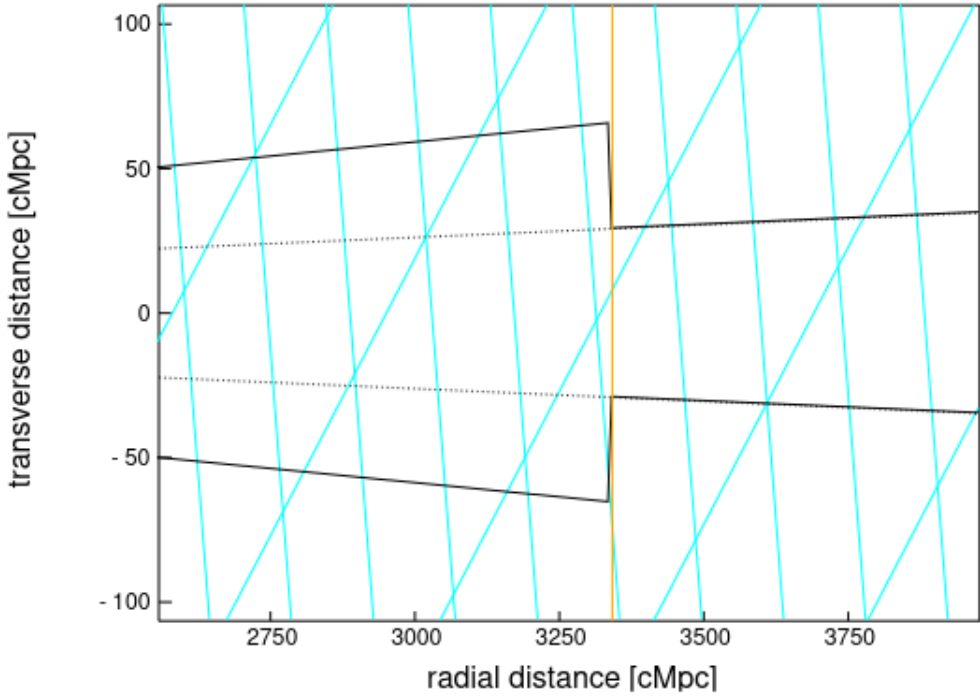


Figure 3.1: Two dimensional graph of the past lightcone generated with Horizon-AGN. Each blue cell is a replicate of the H-AGN simulation box. The orange vertical line marks $z = 1$ and the tiling repeats up to $z = 8$. The black lines represents the aperture angle of the cone which goes from 2.25 arcseconds to 1.00 arcsecond after $z = 1$. Figure extracted from [6]

A raytracing work has been done by C. Gouin et al. in [6], based on similar previous works in the field such as [7]. The idea is that once while the volume is being simulated, we simulate the past lightcone of the observer, represented in figure 3.1. Which means we need to trace the path of light rays that are being deflected by the forefront mass along their journey, from the source to the observer. As explained in C. Gouin's article, this can be done in two different ways, one of them being to integrate the gravitational potential on a thin lens plane, meaning that we dissect our line of sight into different thin lens planes and then integrate the gravitational potential included in each of them.

$$\alpha(\theta) = \frac{2}{c^2} \int \nabla_{\perp} \phi(\theta, x) dx \quad (3.1)$$

3.2 Data definition and analysis

To work on measuring convergence, shear and flexion in the Horizon-AGN simulation, we need to properly define what we want to look out and the procedure in order to do so. We are interested in the galaxy-galaxy lensing statistic. It is a type of weak (although it sometimes falls in the strong regime) gravitational lensing in which a forefront massive galaxy causes

distortions on the shapes of background galaxies/stars. This type of lensing can be used for various interests, for instance :

- Measuring mass density profiles :

Galaxy-galaxy lensing can provide information on the shape of mass profiles. Since lensing doesn't respond to the nature of the mass causing it (it is caused by gravity only), we can probe a very interesting amount of mass environments, like baryons, which proportion tends to dominate at small scales, at the heart of the galaxies, and dark matter, which accumulates in the outer parts of the halos.

- Time evolution:

The mass is not constant throughout the life of a galaxy, thus, focusing the study on different lens populations for different redshifts, we can observe the time evolution of the mass properties of halos.

- Mass-to-light relation:

Not only can we restrict distances and masses, but we can have a look into the average luminosity emitted by a stack of galaxies in specific filters. We recall that since lensing is unaffected by the nature of the matter causing it, the measure would be a virial mass to light ratio. Using then other probes to trace the ratio of baryonic to dark matter will give precious information about the distribution of matter in galactic halos.

We are interested the most in the first bullet point: measuring mass density profiles. To do so, we have at our disposition a selection of the thin lens planes we presented earlier, for each plane we have $2 \times 36\,000 \times 36\,000$ pixels, corresponding to the two different components of the deflection field $\alpha = \alpha_1 + i\alpha_2$, over a square grid of $36\,000 \times 36\,000$ pixels. We will use these maps to compute the convergence, shear, and flexion fields. Recalling eqs. (2.11), (2.12) and (2.16), we express each component in the following table, as derivatives of the deflection field, we detail for instance also how we obtain the expression for κ .

$$\begin{aligned}\kappa &= \frac{1}{2} \partial^* \alpha \\ &= \frac{1}{2} (\partial_1 - i\partial_2)(\alpha_1 + i\alpha_2) \\ &= \frac{1}{2} [(\partial_1 \alpha_1 + \partial_2 \alpha_2) + i(\partial_1 \alpha_2 - \partial_2 \alpha_1)]\end{aligned}\tag{3.2}$$

But since κ is defined to be a scalar, the rotational term or equivalently the complex part of κ needs to be zero, we obtain a relation whose validity will be tested and discussed, as it was in [6],

$$\partial_1 \alpha_2 = \partial_2 \alpha_1\tag{3.3}$$

Computing in a similar manner, we get all of the following expressions that we need for building our lensing quantities maps

$$\begin{aligned}
 \kappa &= \frac{1}{2}(\partial_1 \alpha_1 + \partial_2 \alpha_2) \\
 \gamma_1 &= \frac{1}{2}(\partial_1 \alpha_1 - \partial_2 \alpha_2) \\
 \gamma_2 &= \frac{1}{2}(\partial_1 \alpha_2 + \partial_2 \alpha_1) = \partial_1 \alpha_2 = \partial_2 \alpha_1 \\
 \mathcal{F}_1 &= \frac{1}{2}(\partial_1 \partial_1 \alpha_1 - \partial_1 \partial_2 \alpha_2 + \partial_2 \partial_2 \alpha_1 + \partial_2 \partial_1 \alpha_2) \\
 \mathcal{F}_2 &= \frac{1}{2}(\partial_1 \partial_1 \alpha_2 + \partial_1 \partial_2 \alpha_1 - \partial_2 \partial_1 \alpha_1 + \partial_2 \partial_2 \alpha_2) \\
 \mathcal{G}_1 &= \frac{1}{2}(\partial_1 \partial_1 \alpha_1 - \partial_1 \partial_2 \alpha_2 - \partial_2 \partial_2 \alpha_1 - \partial_2 \partial_1 \alpha_2) \\
 \mathcal{G}_2 &= \frac{1}{2}(\partial_1 \partial_1 \alpha_2 + \partial_1 \partial_2 \alpha_1 + \partial_2 \partial_1 \alpha_1 - \partial_2 \partial_2 \alpha_2)
 \end{aligned} \tag{3.4}$$

Figure 3.2: Expressions as derivatives of the two components of the deflection fields of the seven lensing quantities defined earlier and used

To compute the numerical derivatives, we will use a simple second order finite differences scheme. Now that our quantities are thoroughly defined, we need to correlate the maps (which vary in redshift, as they are different thin lens planes) to the lensed position (equivalently position on the image plan) and appearance of the galaxies extracted from a catalog built from the simulated lightcone defined earlier. To do so, we need to define what we call the tangential component of all the lensing fields. Talking about tangential convergence has no sense, as it is a scalar, so its projection on the tangential direction is simply itself. But for all of the other lensing component, we need to take the real part of each lensing component λ_i , and we define

$$\lambda_{i+} = \Re(\lambda_i \cdot e^{n_i \pi \phi}), \forall (\lambda_i, n_i) \in [(\gamma, 2), (\mathcal{F}, 1), (\mathcal{G}, 3)] \tag{3.5}$$

Proceeding to such a projection, we get the following expressions for each component we need to measure. It will also be interesting to study the cross lensing components, as opposed to the tangential ones, which are defined as their imaginary part.

$$\begin{aligned}
 \kappa_+ &= \kappa & (3.6) \\
 \gamma_+ &= -\gamma_1 \cos(2\phi) - \gamma_2 \sin(2\phi) = -\gamma_1(\cos^2(\phi) - \sin^2(\phi)) - \gamma_2 \cdot 2 \sin(\phi) \cos(\phi) \\
 \mathcal{F}_+ &= -\mathcal{F}_1 \cos(\phi) - \mathcal{F}_2 \sin(\phi) \\
 \mathcal{G}_+ &= -\mathcal{G}_1(4 \cos^3(\phi) - 3 \cos(\phi)) - \mathcal{G}_2(4 \sin^3(\phi) - 3 \sin(\phi))
 \end{aligned}$$

Figure 3.3: Tangential projection of the lensing quantities, generated by gravitational lensing, used to effectively compute and measure the lensing quantities.

Those tangential expressions were obtained by using eq.(3.5), and then reexpressing the components as functions of ϕ rather than $n\phi$. The following cross lensing quantities are not generated by gravitational lensing, so measuring them should give no signal; doing so is a great way of checking for systematics.

$$\begin{aligned}
 \gamma_x &= \gamma_1 \sin(2\phi) - \gamma_2 \cos(2\phi) = \gamma_1 2 \sin(\phi) \cos(\phi) - \gamma_2 (\cos^2(\phi) - \sin^2(\phi)) & (3.7) \\
 \mathcal{F}_x &= \mathcal{F}_1 \sin(\phi) - \mathcal{F}_2 \cos(\phi) \\
 \mathcal{G}_x &= -\mathcal{G}_2(4 \cos^3(\phi) - 3 \cos(\phi)) + \mathcal{G}_1(-4 \sin^3(\phi) + 3 \sin(\phi))
 \end{aligned}$$

Figure 3.4: Cross projection of the lensing quantities, which should yield no signal and thus can be used as a robust way of checking for systematical errors.

Eq. (3.6) can be re-expressed in a final way, using the x,y coordinates on the sky plane, considered flat because we know that the lightcone is opened with a 2.25° angle until redshift 1, and 1° afterwards, since the angles are small relative to the distances, we can easily compute the angular diameter distance. Samely with eq. (3.7).

$$\begin{aligned}
 \gamma_+ &= -\gamma_1 \frac{x^2 - y^2}{r^2} - \gamma_2 \frac{2xy}{r^2} & (3.8) \\
 \mathcal{F}_+ &= \frac{-\mathcal{F}_1 x - \mathcal{F}_2 y}{r} \\
 \mathcal{G}_+ &= -\mathcal{G}_1 \left(4 \frac{x^3}{r^3} - 3 \frac{x}{r} \right) - \mathcal{G}_2 \left(4 \frac{y^3}{r^3} - 3 \frac{y}{r} \right)
 \end{aligned}$$

Figure 3.5: Tangential projection of the lensing quantities, expressed in flat sky plane coordinate.

$$\begin{aligned}\gamma_x &= \gamma_1 \frac{2xy}{r^2} - \gamma_2 \frac{x^2 - y^2}{r^2} \\ \mathcal{F}_x &= \frac{\mathcal{F}_1 y - \mathcal{F}_2 x}{r} \\ \mathcal{G}_x &= -\mathcal{G}_2 \left(4 \frac{x^3}{r^3} - 3 \frac{x}{r} \right) + \mathcal{G}_1 \left(4 \frac{y^3}{r^3} - 3 \frac{y}{r} \right)\end{aligned}\tag{3.9}$$

Figure 3.6: Cross projection of the lensing quantities, expressed in flat sky plane coordinates.

All of those formulas allow us to measure correctly the flexion, shear and convergence in our simulated lightcone data from the Horizon-AGN simulation.

3.3 Mass density profiles

We now need to define the various mass density profiles we will use to fit our gravitational lensing measurements and thus derive from their original expressions, the formulas for convergence κ , shear γ and the two flexion fields \mathcal{F} and \mathcal{G} .

3.3.1 The Singular Isothermal Sphere (SIS) model

This model is by far one of the simplest ones we can study, as it only implies that the mass density profile scales as the inverse of the square of the distance from the lens' center.

$$\rho \propto \frac{1}{r^2}\tag{3.10}$$

This type of profile, presented for instance in [8] is obtained by considering constant velocity dispersion for the dark matter particles all around the matter halo. Defining the projected surface mass density of the SIS,

$$\Sigma(\xi) = \frac{\sigma_v^2}{2G\xi}\tag{3.11}$$

where ξ is the distance from the center of the lens and σ_v the velocity dispersion aforementioned. Since the convergence is defined as $\kappa = \Sigma/\Sigma_c$, with Σ_c the critical density,

$$\Sigma_c = \frac{c^2}{4\pi G} \frac{D_s}{D_l D_{ls}}\tag{3.12}$$

with D_s, D_l and D_{ls} respectively the angular diameter distance from observer to source, observer to lens, lens to source, we obtain finally for κ ,

$$\kappa(\theta) = \frac{\theta_E}{2\theta} \quad (3.13)$$

θ_E is called the Einstein angle and θ is the angular distance to the center of the lens, defined respectively as,

$$\begin{aligned} \theta &= \frac{\xi}{D_l} \\ \theta_E &= 4\pi \frac{D_{ls}}{D_s} \frac{\sigma_v^2}{c^2} \end{aligned} \quad (3.14)$$

As derived in [9], the shear caused by such a mass profile is,

$$\gamma(\theta) = -\frac{\theta_E}{2\theta} e^{2i\phi} \quad (3.15)$$

where we recall that as is eqs. (3.5), (3.6) and (3.7) ϕ is the angle around the lens. We can finally express the flexion components,

$$\begin{aligned} \mathcal{F} &= -\frac{\theta_E}{2\theta^2} e^{i\phi} \\ \mathcal{G} &= \frac{3\theta_E}{2\theta^2} e^{3i\phi} \end{aligned} \quad (3.16)$$

where we recover properly the spin properties we talked about when introducing the two different flexion fields. We see that fitting using the SIS model, we have only one free parameter, θ_E , for the four different lensing fields, we will see the implications and differences with the next model in section 4.

3.3.2 The Navarro-Frenk-White (NFW) model

This model quickly raises complexity in its expression, and especially when expressing the lensing components. This model was empirically found and studied by the three scientists that gave the model its name, Julio Navarro, Carlos Frenk and Simon White in [10]. The mass density is given by the following formula,

$$\rho(x, z) = \frac{\Delta_c \rho_c(z)}{x(1+x)^2} \quad (3.17)$$

where $x = r/r_s$ is the distance to the center, in units of a characteristic radius r_s , one of the free parameters of the model, $\rho_c(z)$ is the critical density at redshift z and Δ_c is a unit-less scaling

density which is a function of another free parameter, c the concentration of the halo,

$$\Delta_c = \frac{200}{3} \frac{c^3}{\ln(1+c) - \frac{c}{1+c}} \quad (3.18)$$

for this profile, the convergence can be written as a complicated function of a new variable $y = \xi/r_s$

$$\kappa(y) = 2\kappa_s \frac{f(y)}{y^2 - 1} \quad (3.19)$$

where κ_s is related to the other constants as $\kappa_s = \rho_c(z)\Delta_c r_s/\Sigma_c$ and the function $f(y)$ is given by

$$f(y) = \begin{cases} 1 - \frac{2}{\sqrt{1-y^2}} \operatorname{arctanh} \sqrt{\frac{1-y}{1+y}} & y < 1 \\ 1 - \frac{2}{\sqrt{y^2-1}} \operatorname{arctan} \sqrt{\frac{y-1}{y+1}} & y > 1. \end{cases} \quad (3.20)$$

The shear is given by the following formula,

$$\gamma(y) = \kappa_s g(y) \quad (3.21)$$

where,

$$g(y) = \begin{cases} \frac{8 \operatorname{arctanh} \sqrt{(1-y)/(1+y)}}{y^2 \sqrt{1-y^2}} + \frac{4}{y^2} \ln \left(\frac{y}{2}\right) - \frac{2}{(y^2-1)} + \frac{4 \operatorname{arctanh} \sqrt{(1-y)/(1+y)}}{(y^2-1)(1-y^2)^{1/2}} & y < 1 \\ \frac{10}{3} + 4 \ln \left(\frac{1}{2}\right) & y = 1. \\ \frac{8 \operatorname{arctan} \sqrt{(y-1)/(1+y)}}{y^2 \sqrt{y^2-1}} + \frac{4}{y^2} \ln \left(\frac{y}{2}\right) - \frac{2}{(y^2-1)} + \frac{4 \operatorname{arctan} \sqrt{(y-1)/(1+y)}}{(y^2-1)^{3/2}} & y > 1 \end{cases} \quad (3.22)$$

and the flexion fields are given by

$$\begin{aligned} \mathcal{F}(y, \phi) &= -\frac{2\mathcal{F}_s}{(y^2-1)^2} [2yf(y) - h(y)] e^{i\phi} \\ \mathcal{G}(y, \phi) &= 2\mathcal{F}_f \left[\frac{8}{y^3} \ln \frac{y}{2} + \frac{(3/y)(1-2y^2) + j(y)}{(y^2-1)^2} \right] e^{3i\phi} \end{aligned} \quad (3.23)$$

where the functions $h(y)$ and $j(y)$ are given by

$$h(y) = \begin{cases} \frac{2y}{\sqrt{1-y^2}} \operatorname{arctanh} \sqrt{\frac{1-y}{1+y}} - \frac{1}{y}, & y < 1 \\ \frac{2y}{\sqrt{y^2-1}} \operatorname{arctan} \sqrt{\frac{y-1}{y+1}} - \frac{1}{y}, & y > 1. \end{cases} \quad (3.24)$$

$$j(y) = \begin{cases} \left(\frac{8}{y^3} - \frac{20}{y} + 15y\right) \frac{2}{\sqrt{1-y^2}} \operatorname{arctanh} \sqrt{\frac{1-y}{1+y}} & \text{if } y < 1 \\ \left(\frac{8}{y^3} - \frac{20}{y} + 15y\right) \frac{2}{\sqrt{y^2-1}} \operatorname{arctan} \sqrt{\frac{y-1}{y+1}} & \text{if } y > 1 \end{cases} \quad (3.25)$$

and $\mathcal{F}_s = \kappa_s D_l / r_s$. It is worth to note that the variables y and ϕ are decoupled, and since we are only interested for now in the radial mass profile, we can simply integrate over a full turn around the lens to "free" the formulas of their angular components.

3.4 Numerical lensing measurement

Let us explain how we measure lensing in practice. Given a catalog of the galaxies present in the Horizon-AGN lightcone, we have at our disposition a list of parameters for each galaxy.

Column Name	Description
MVIRH_MAIN	Main virial mass of the halo
RA_IMG	Right ascension of the galaxy image
MTOTH_SUB	Total mass of the subhalo
CHECK	Quality check flag
DEC	Declination
RA	Right ascension
MTOTH_MAIN	Total mass of the main halo
IDH_MAIN	Main halo ID
ID_PHOTOOMETRY	Photometry ID
ES2	Ellipticity component s2
E1	Ellipticity component e1
GAMMA2	Shear component gamma2
ID	Unique galaxy ID
MASS_TRUE	True mass of the galaxy
ID_HzAGNFULL	ID in the HzAGN full simulation
E2	Ellipticity component e2
MAGNIF	Magnification due to lensing
ES1	Ellipticity component s1
z_true	True redshift
KAPPA	Convergence
MVIRH_SUB	Virial mass of the subhalo
GAMMA1	Shear component gamma1
DEC_IMG	Declination of the galaxy image
IDH_SUB	Subhalo ID

Table 3.2: Available information in the header of the galaxy catalog within the Horizon-AGN simulated light cone.

Since we are interested in gravitational lensing and the influence of redshift and mass on it, we will mainly be interested in the following columns :

- RA_IMG, the lensed right ascension coordinate of the galaxy
- DEC_IMG, the lensed declination coordinate of the galaxy
- z_true, the galaxy's redshift in the simulated lightcone
- MTOTH_MAIN, the total mass of the main dark matter halo in which the galaxy is contained
- MTOTH_SUB, the total mass of the possible dark matter sub-halo that the galaxy represents
- IDH_SUB, the unique ID of the aforementioned possible sub-halo
- IDH_MAIN. the unique ID of the main halo containing the galaxy

When we say "possible dark matter sub-halo", we mean that we can divide the galaxies into two categories, the main and satellite galaxies. The first category represents the galaxies with the largest halos, that tend to "host" other substructures, so called sub-halos, or satellite galaxies. To do such a categorization, we compare if for a given galaxy, its IDH_SUB is equal to its IDH_MAIN, if its equal, then the galaxy is its own main halo, it is a main or host galaxy. If not, then it is comprised within a larger dark matter halo, it is a satellite galaxy.

We also need to sort the galaxies by redshift. We are given a handful of thin lens planes which are to be interpreted as an integral of all the forefront mass between the observer and the corresponding redshift of the thin lens plane in question. A known result in lensing physics is that the usual deflectors are located for a given source at around half the physical distance, as specified in [11]. This means that for a given plane, we compute the comoving distance, half it and then compute the redshift corresponding to this comoving distance, taking a slice of arbitrary width around this redshift (± 0.1 in our case) allows us to minimize noise from galaxies that wouldn't interfere with the given lens system, as they would be too far or too close from the observer, while keeping a significant and satisfying amount of signal to work with.

Once those two selections are done, we sort by mass, i.e. taking a specific range of galaxy masses, be it the 500 most massive, or 500 least massive, to see the influence of mass on the lensing signal. Now, for a given plane, our galaxies are correctly sorted and selected, we can go on and measure the convergence, shear and flexion signals. To do so, we iterate over the selected galaxies, and draw concentric circles around each galaxy, as to divide its surrounding space in radii bins.

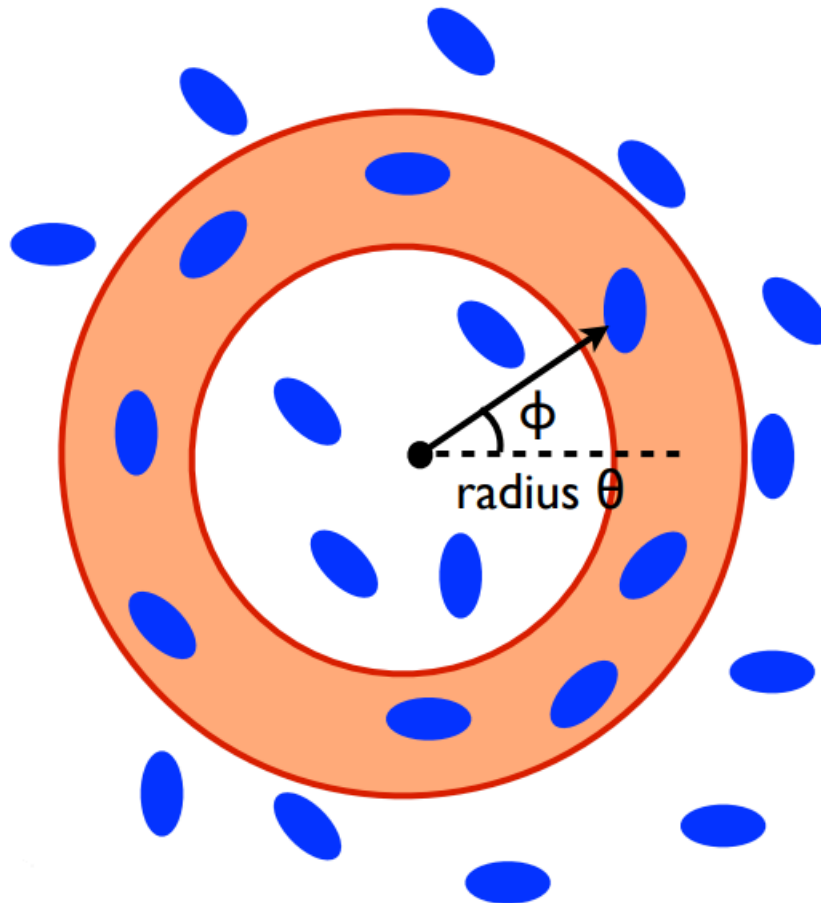


Figure 3.7: The process of measuring the galaxy-galaxy lensing correlation statistic. Figure by Masamune Oguri

Doing so, we can sort the pixels of the convergence/shear/flexion maps, computed with Eq. (3.4) into the corresponding bins, and add successively the values of the tangential components, defined in Eq. (3.8), then dividing each components' bins by the numbers of pixels in it. This will allow us to finally have a measurement of gravitational lensing caused by galaxies on other galaxies by applying this process on all the lensing fields.

CHAPTER 4

Results and interpretation

This section will focus on a detailed analysis of measurements resulting from the framework described earlier. We aim to present the data collected, followed by an interpretation of what the results signify in the context of the study. Each subsection will address specific checkpoints of the internship and situate it in regards to the set objective. The purpose is to provide a comprehensive understanding of the outcomes, bridging the gap between raw data and its implications for the rest of the work.

4.1 Tools and discussion

4.1.1 Julia

We will use the language Julia for the purpose of our work. Choosing between Julia, Python, C, or C++ (among others) involves considering factors such as performance, ease of use, available libraries, the ability to interface between them, and specific use cases. Julia offers high performance close to C, thanks to JIT compilation, making it ideal for numerical computation and scientific computing. It's user-friendly like Python, with a syntax conducive to mathematical operations, but its ecosystem, though growing, isn't as extensive as Python's.

Python is most likely the best in readability and simplicity, supported by a vast ecosystem specialized in data analysis, machine learning, and web development. It is versatile, with the ability to call C/C++ for performance tasks, but it generally offers slower execution speed.

C and C++ are known for their high performance and control over system resources, which makes them suitable for system-level programming and applications that require maximum efficiency. However, they have a steeper learning curve and more complex syntax compared to Julia and Python, which can slow down development and hinder its readability.

For all these reasons, Julia is a strong candidate for projects that demand high computational performance and mathematical modeling like ours.

4.1.2 Error estimation

To estimate the error bars in the measurements of convergence, shear and flexion, we will use a Jackknife resampling. The decision between using the jackknife rather than other statistical

methods to estimate error bars is based on various factors related to the data and the objectives of the analysis. The Jackknife method is known for its computational simplicity and speed, which makes it particularly suitable for large datasets because of its methodical approach of excluding one (or more, in the case of block Jackknife) observation at a time. This method not only facilitates bias correction, but is also a simple tool for variance estimation, ensuring our ability to reproduce our results.

However, one might want to use the bootstrap, which is a pretty flexible tool. It allows for intensive replacement resampling, creating numerous samples that effectively simulate drawing new samples from the population. This method is particularly beneficial for complex estimators, where it can provide more accurate error estimates by capturing the estimator's distribution more comprehensively. Despite being computationally intensive, bootstrap methods are relatively straightforward to implement and can be adapted to various estimators and statistical measures.

Since our estimators are simple in nature and our samples are large but somewhat reasonable when it comes to computing power needed to treat them, we will settle on the Jackknife resampling.

4.2 Thin lens planes and lensing maps

As mentioned earlier, we have at our disposition a selection of thin lens planes, each containing information such as their redshift, and two 36 000 pixels x 36 000 pixels maps, representing the two independent deflection fields α_1 and α_2 , recalling Eq. (2.10). By Eq. (3.4), and using a second order finite difference differentiation scheme, we can easily compute each of the lensing maps $\kappa, \gamma_1, \gamma_2, \mathcal{F}_1, \mathcal{F}_2, \mathcal{G}_1$ and \mathcal{G}_2 . We recall that since the angles are small the plane is considered flat, and thus the derivatives are to be taken cartesian and one can understand ∂_1 , the derivative with respect to the first coordinate, as $\partial/\partial x$ the derivative with respect to the x coordinate, and samely with ∂_2 as $\partial/\partial y$.

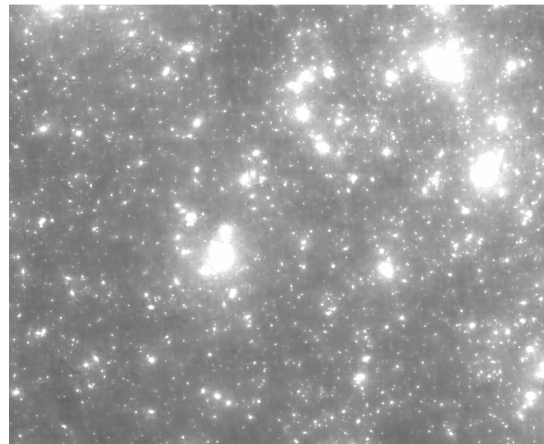
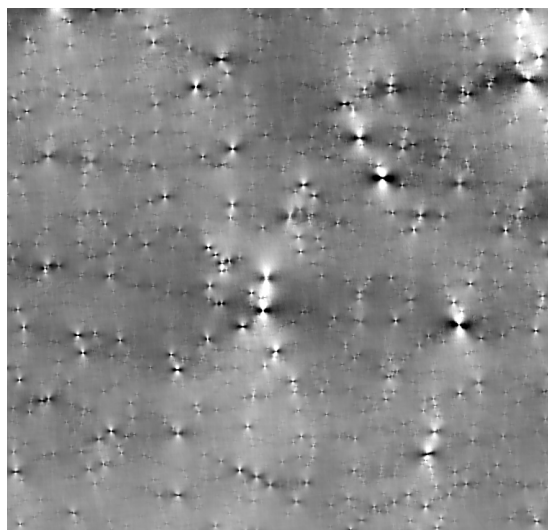
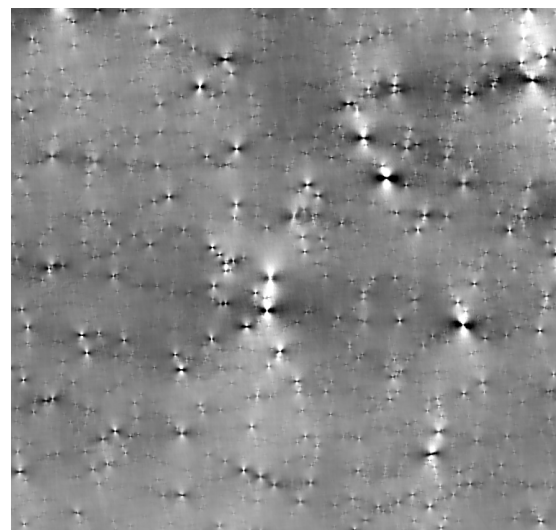


Figure 4.1: Convergence map for a redshift $z_{plane} \approx 1.016$, computed from a combination of derivatives of the two deflection field maps.

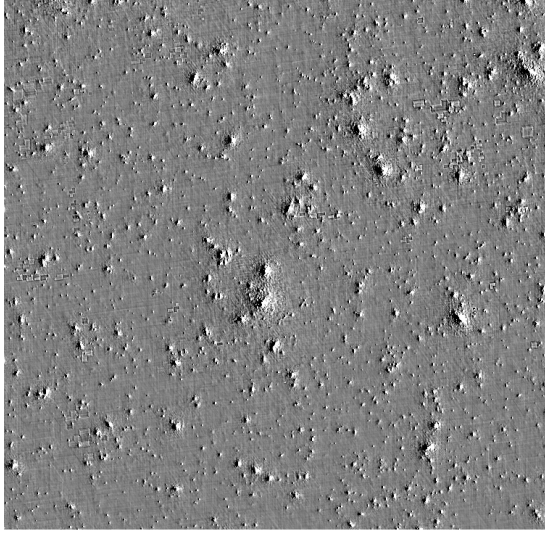


(a) γ_1 shear map, with its visible spin 2 property

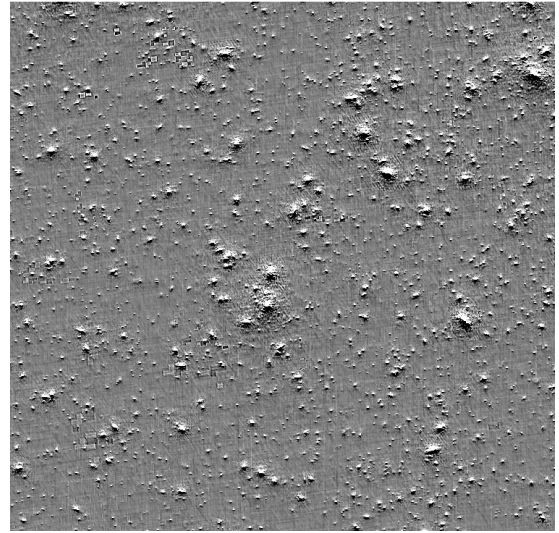


(b) γ_2 shear map, one can notice that it is seemingly the same as γ_1 but rotated 90°

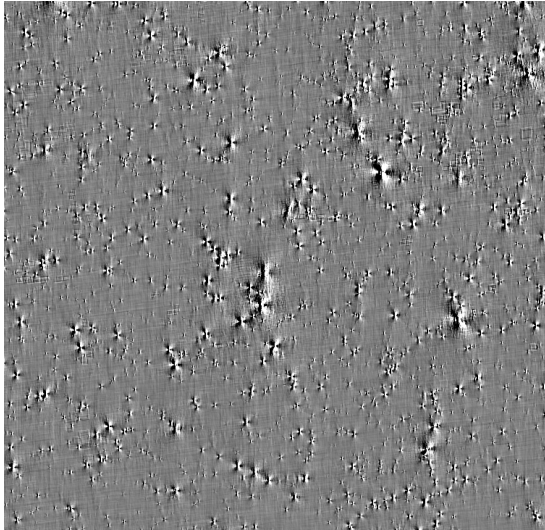
Figure 4.2: The two different shear fields γ_1 and γ_2



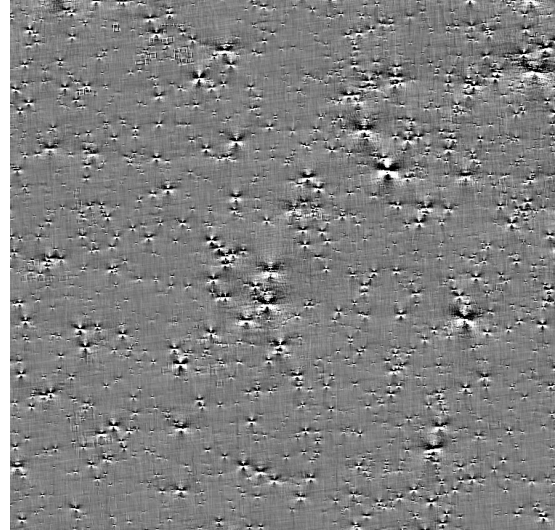
(a) \mathcal{F}_1 flexion map, with its visible spin 1 property



(b) \mathcal{F}_2 flexion map, one can notice that it is seemingly the same as \mathcal{F}_1 but rotated 90°



(c) \mathcal{G}_1 flexion map, and its noticeable spin 3 property



(d) \mathcal{G}_2 flexion map, also seems to be like \mathcal{G}_1 but rotated 90°

Figure 4.3: The four different flexion fields $\mathcal{F}_1, \mathcal{F}_2$ and $\mathcal{G}_1, \mathcal{G}_2$. Computed by the code in Appendix A.

These different maps were computed for every single deflection map, and then used to apply the process of averaging the signal in radii bins around the galaxies of the lightcone catalog. Doing so we get the results presented in the following section.

4.3 Numerical correlation computation and results

The whole code that was used for those computations can be found in Appendix B.

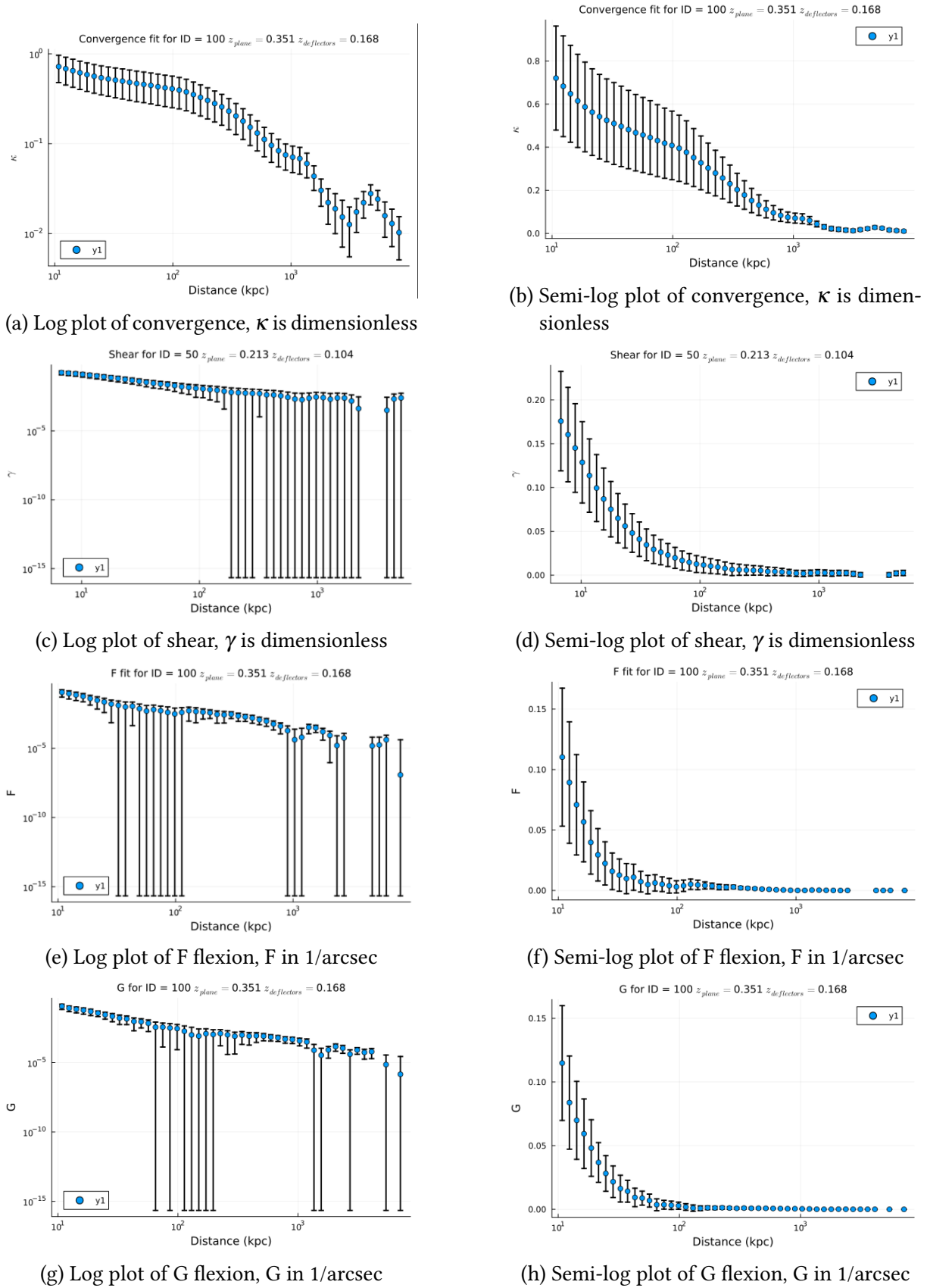


Figure 4.4: Galaxy-Galaxy lensing correlations for each component and arbitrary lens planes

The previous figure stands to show some first approach to the lensing signal, for each component, convergence, tangential shear, tangential 1-flexion and 3-flexion. With on the left the loglog plots, and since for some radii bins, the signal gets too close to zero (but since we don't want to introduce some bias in our analysis, we get rid of bins where the signal goes lower than zero, which explains for example the missing points in panel (c), (d), (e) and (f) of the figure) the error bars get stretched out, so we included the right panels in semi-log for better visibility of the signal.

4.4 The difference between satellite and central galaxies

Central galaxies are the primary galaxies located at the center of their dark matter halos. They typically reside in the most massive and densest part of the halo.

- **1-Halo Term:** For central galaxies, the 1-halo term dominates at small scales, showing a strong lensing signal due to the dense dark matter distribution around the central galaxy. This signal reflects the mass profile of the entire halo, including any substructures like satellite galaxies within the same halo. We expect the lensing signal for central galaxies to be maximal at small separations from the galaxy and continuously decrease with a relatively steep slope (compared to the satellites) towards a stable value at large scales, where the 2-halo term now dominates.
- **2-Halo Term:** At larger scales, the 2-halo term takes over, reflecting the contribution from neighboring halos. Beyond a few hundred kiloparsecs, flattens out and extends, indicating the influence of nearby halos and the large-scale structure.

On the other hand, satellite galaxies are those that orbit within the halo of a larger central galaxy. They are not at the center of the halo and typically inhabit the outer regions.

- **1-Halo Term:** For satellite galaxies, the 1-halo term still contributes at small scales, but it reflects the dark matter distribution around the satellite within the larger halo of the central galaxy. The lensing signal at small scales for satellite galaxies is expected to decrease with a softer slope compared to central galaxies, because it represents the less dense outer regions of the halo where satellites reside. The peak of the 1-halo term may also shift slightly outward compared to central galaxies, because the main halo is thus in the surroundings of the satellite.
- **2-Halo Term:** Similar to central galaxies, the 2-halo term for satellites becomes significant at larger scales. The larger scale lensing signal will again show a flatter extension, indicating the influence of surrounding halos. However, this signal might be somewhat weaker compared to that of central galaxies due to the satellite's position within the larger halo.

Chapter 4: Results and interpretation

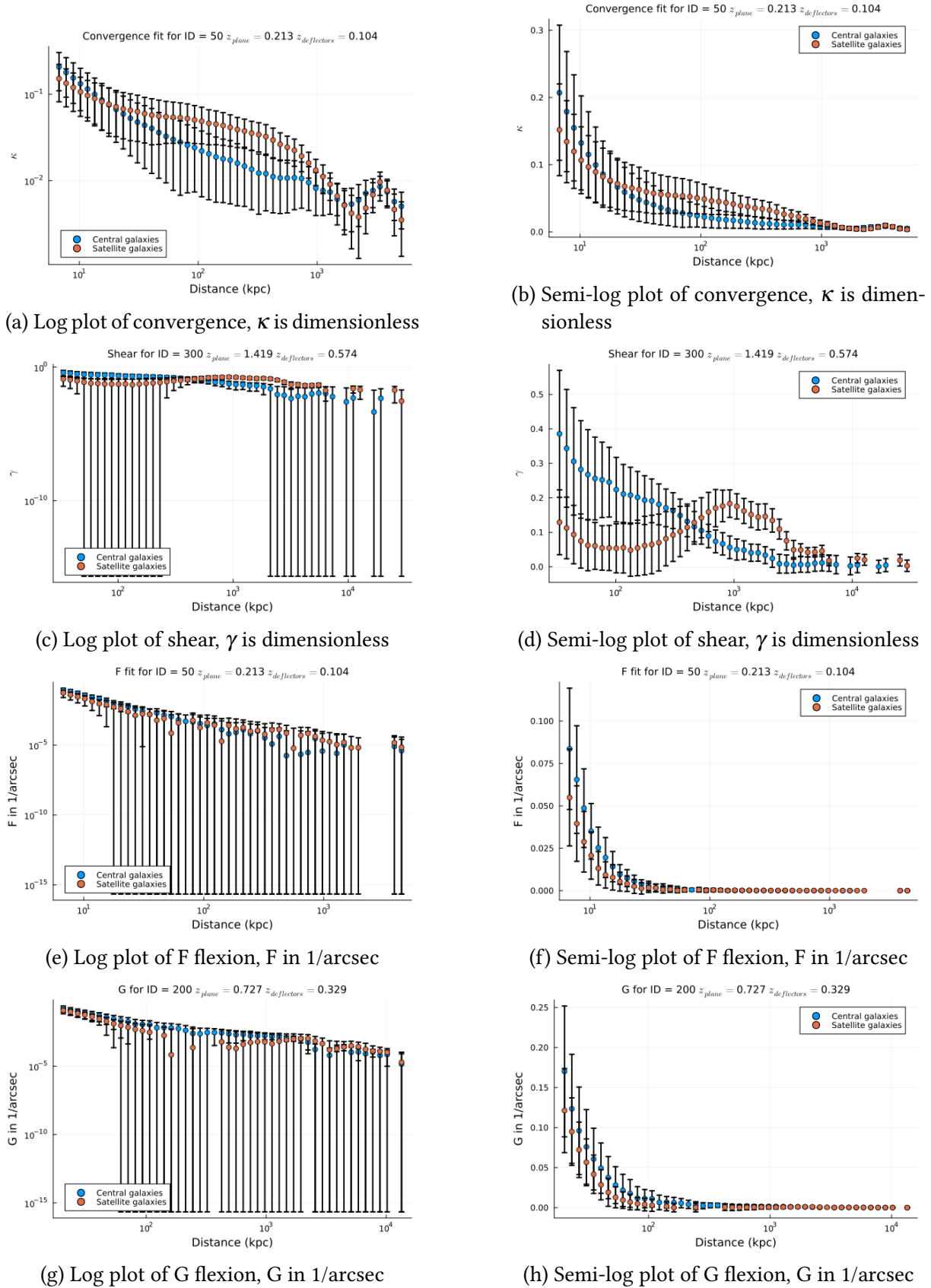


Figure 4.5: Galaxy-Galaxy lensing correlations for each component and arbitrary lens planes

We see that indeed, for satellite galaxies, the signal decreases slower than for the central ones, with some sort of "bump" visible towards the middle scales, due to the effects described earlier, the satellite galaxies, located in the outer part of the halos, cause signal further away due to the proximity of the main halo.

4.5 Fitting the SIS and NFW models

4.5.1 Central galaxies

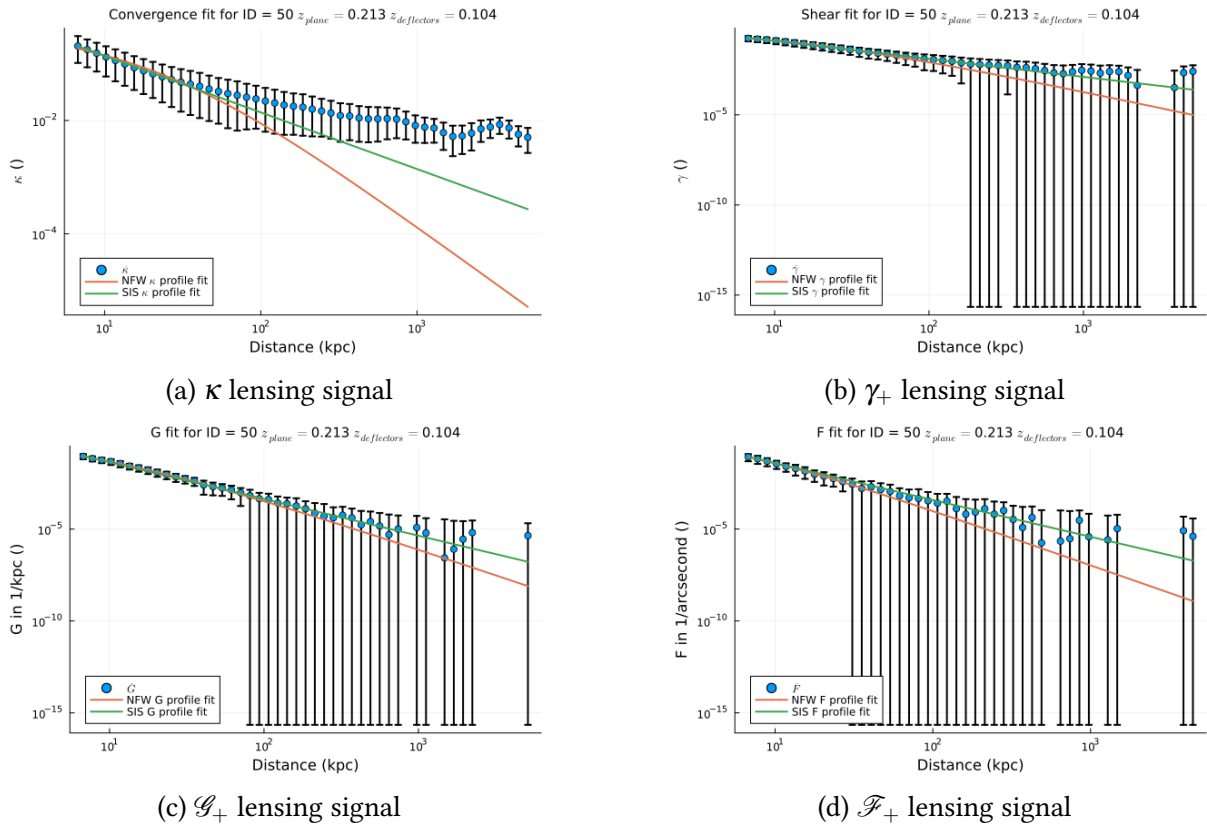


Figure 4.6: Lensing signals for each component, fitted with the SIS and NFW models. Computed by the code in Appendix B.

For information, we fit the models with a certain cutoff radius set arbitrarily, because we want to restrict the models to the one-halo term. Here, the radius cutoff has been chosen to be around 800 kpc. We do the same fits for the satellite galaxies.

4.5.2 Satellite galaxies

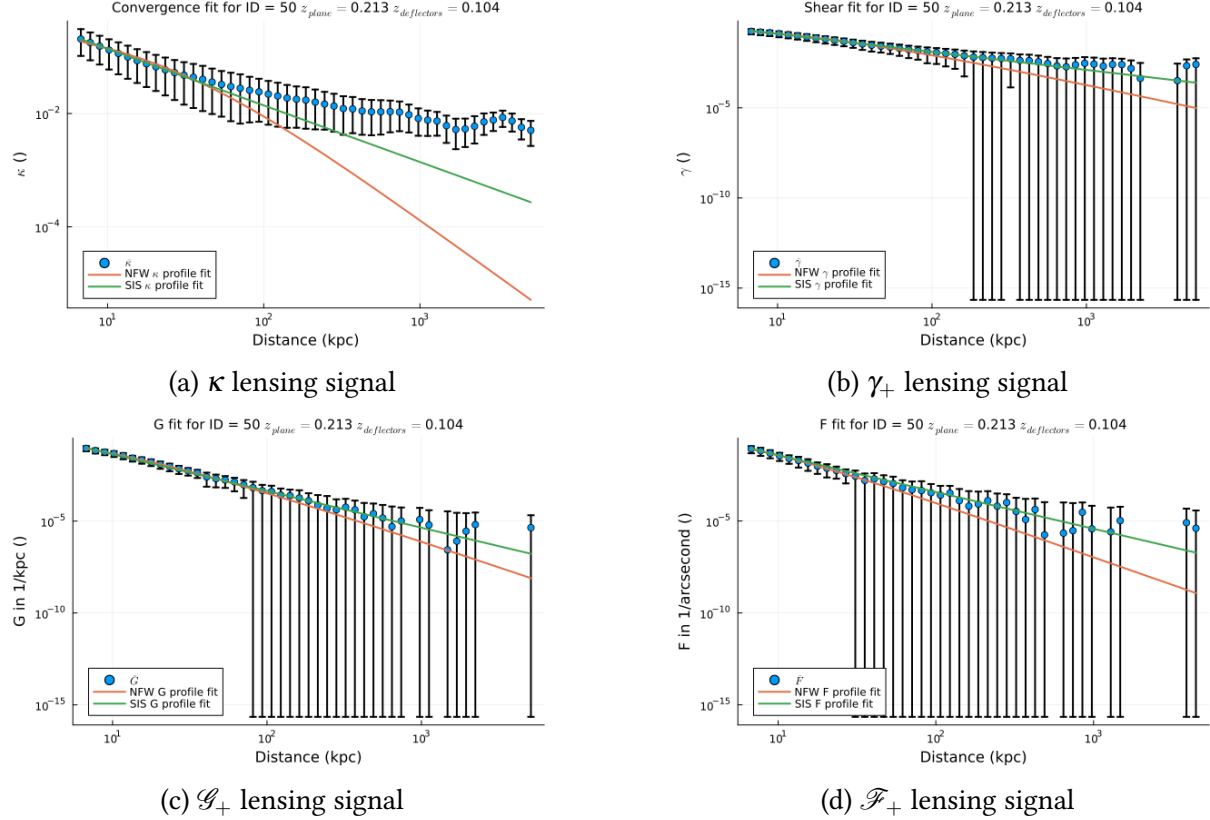


Figure 4.7: Lensing signals for each component, fitted with the SIS and NFW models. Computed by the code in Appendix B.

CHAPTER 5

Euclid, SourceExtractor++ and Machine Learning

As a quick complement before ending this report, this section stands to present the rest of the work that will be done during the time that lasts between the submission and the end of this internship. Now that the flexion signal has been studied, measured and understood in the Horizon-AGN simulated data, we want to apply the measurement process on actual sources from the Euclid survey. To do so, we will use the SourceExtractor++ software.

5.1 The Euclid Survey

The Euclid satellite is a mission led by the European Space Agency (ESA) with the primary objective of mapping the geometry of the dark universe. Launched to observe billions of galaxies over more than a third of the sky, Euclid aims to investigate the nature of dark energy and dark matter, which together constitute about 95% of the universe's mass-energy content.

Let us recall that Euclid is equipped with a visible imaging channel (VIS) and a near-infrared spectrometer and photometer (NISP) thanks to which it will measure the shapes and redshifts of distant galaxies with unprecedented precision. By doing so, it will provide crucial data for understanding the expansion history of the universe and the growth of cosmic structures.

Euclid's data will enable scientists to test theories of gravity on cosmic scales, offering insights into fundamental questions about the nature of the universe. The mission's comprehensive sky survey and its ability to combine multiple observational techniques make it a huge project for cosmology and astrophysics in the coming decade.

5.2 SourceExtractor++

SourceExtractor++ (also known as SExtractor++ or SEPP) is a state-of-the-art tool designed for extracting and analyzing sources such as stars and galaxies from astronomical images. It enhances the older SourceExtractor (SExtractor) software, providing superior features for analyzing astronomical data. The software boosts performance through multi-threading and

parallel processing, making it efficient in handling large datasets. Improved memory management further aids in processing large-scale images and complex datasets. SourceExtractor++ features advanced detection algorithms to accurately identify faint and overlapping sources, while reducing noise and background fluctuations in astronomical images. A key benefit of SourceExtractor++ is its modularity, which allows users to customize and expand the software according to their specific requirements. This flexibility is supported by various plug-ins that increase functionality and adaptability. SourceExtractor++ can output data in multiple formats, ensuring integration with other software and processing workspaces. The software produces detailed catalogs of detected sources, covering a wide range of characteristics and parameters. It is widely used in significant astronomical surveys to identify and catalog celestial objects and is applicable to any project requiring source extraction and analysis from image data. The software delivers highly accurate source extraction and access to photometry information on the sources. Its high-performance capability allows for the processing of large datasets within feasible timeframes, while its modular design and customization options accommodate diverse research needs. We mentionned that SEPP was an upgrade from SE, via the use of multithreading for instance, but we are most interested in its compatibility with the ONNX framework, which will allow us to modify SEPP "from outside", since it is a complicated software written mainly in C++, we don't want to do the dirty work of rewriting by hand the new flexion parameters that need to be fitted.

5.3 ONNX

ONNX, which stands for Open Neural Network Exchange, is an open-source format designed to represent machine learning models. ONNX provides tools to interchange models between different deep learning frameworks. It facilitates model portability and deployment across various platforms, thereby promoting interoperability in the ecosystem of machine learning tools. Integrating ONNX with SourceExtractor++ will allow us to enhance the capabilities of the software, especially in source shape measurement, incorporating flexion terms in SEPP, without having to modify the source code. Using a deep learning framework like PyTorch or TensorFlow will allow us to convert a trained model to the ONNX format. Since SEPP is already compatible with ONNX, the work will lie in our capacity to create the first model and then validating it with data.

CHAPTER 6

Conclusion and Future Work

Bibliography

- [1] M. Meneghetti, *Introduction to Gravitational Lensing With Python Examples*, vol. 956. 2021. → [p4]
- [2] D. J. Bacon, D. M. Goldberg, B. T. P. Rowe, and A. N. Taylor, “Weak gravitational flexion,” , vol. 365, pp. 414–428, Jan. 2006. → [p6], [p7], [p41]
- [3] Y. Dubois, C. Pichon, C. Welker, D. Le Borgne, J. Devriendt, C. Laigle, S. Codis, D. Pogosyan, S. Arnouts, K. Benabed, E. Bertin, J. Blaizot, F. Bouchet, J. F. Cardoso, S. Colombi, V. de Lapparent, V. Desjacques, R. Gavazzi, S. Kassin, T. Kimm, H. McCracken, B. Milliard, S. Peirani, S. Prunet, S. Roubert, J. Silk, A. Slyz, T. Sousbie, R. Teyssier, L. Tresse, M. Treyer, D. Vibert, and M. Volonteri, “Dancing in the dark: galactic properties trace spin swings along the cosmic web,” , vol. 444, pp. 1453–1468, Oct. 2014. → [p8]
- [4] R. Teyssier, “Cosmological hydrodynamics with adaptive mesh refinement. A new high resolution code called RAMSES,” , vol. 385, pp. 337–364, Apr. 2002. → [p8]
- [5] E. F. Toro, M. Spruce, and W. Speares, “Restoration of the contact surface in the HLL-Riemann solver,” *Shock Waves*, vol. 4, pp. 25–34, July 1994. → [p8]
- [6] C. Gouin, R. Gavazzi, C. Pichon, Y. Dubois, C. Laigle, N. E. Chisari, S. Codis, J. Devriendt, and S. Peirani, “Weak lensing in the Horizon-AGN simulation lightcone. Small-scale baryonic effects,” , vol. 626, p. A72, June 2019. → [p9], [p10], [p41]
- [7] M. Petkova, R. B. Metcalf, and C. Giocoli, “glamer – II. Multiple-plane gravitational lensing,” *Monthly Notices of the Royal Astronomical Society*, vol. 445, pp. 1954–1966, 10 2014. → [p9]
- [8] J. Binney and S. Tremaine, *Galactic dynamics*. 1987. → [p13]
- [9] M. Bartelmann and P. Schneider, “Weak gravitational lensing,” *Physics Reports*, vol. 340, p. 291–472, Jan. 2001. → [p14]
- [10] J. F. Navarro, C. S. Frenk, and S. D. M. White, “The Structure of Cold Dark Matter Halos,” , vol. 462, p. 563, May 1996. → [p14]
- [11] B. Jain and U. Seljak, “Cosmological model predictions for weak lensing: Linear and nonlinear regimes,” *The Astrophysical Journal*, vol. 484, p. 560–573, Aug. 1997. → [p17]

CHAPTER 7

Appendix

A Julia code for computing the lensing maps

The following Julia functions are : `alpha2jac()` used to compute the Jacobian matrix of the source-image coordinate transformation, and the various `jac2...()` functions, such as `jac2kappa()` that take as input the Jacobian computed in `alpha2jac()` and transform it into the lensing maps for each quantity, as well as some extra maps such as the rotational map, which will allow us to verify that Eq. (3.3) is verified, computed with `jac2rot()`, we will also check that our numerical derivatives commute correctly, thanks to `jac2crossderivative1()` and `jac2crossderivative2()`

```
function alpha2jac( alpha::Array{Float32,3} ; scale::Float32=1.0f0 )
    nn = size(alpha)
    (nn1::Int64,nn2::Int64) = (nn[1],nn[2])
    (conv1,conv2) = (nn1/scale, nn2/scale)
    jac = Array{Float32,3}(undef,nn1,nn2,12)
    d = Array{Float32,1}(undef, nn1)
    dd = Array{Float32,1}(undef, nn1)
    ddd = Array{Float32,1}(undef, nn1)

    ## Computing d1a1 and d1d1a1
    @inbounds for j=1:nn2
        @inbounds @simd for i=1:nn1
            d[i] = alpha[i,j,1] * conv1
        end
        deriv!( d, dd )
        deriv!( dd, ddd )
        @inbounds @simd for i=1:nn1
            jac[i,j,1] = dd[i]
            jac[i,j,5] = ddd[i]
        end
    end
end
```

```
## Computing d1a2 and d1d1a2
@inbounds for j=1:nn2
    @inbounds @simd for i=1:nn1
        d[i] = alpha[i,j,2] * conv1
    end
    deriv!( d, dd )
    deriv!( dd, ddd )
    @inbounds @simd for i=1:nn1
        jac[i,j,2] = dd[i]
        jac[i,j,6] = ddd[i]
    end
end

d = Array{Float32,1}(undef, nn2)
dd = Array{Float32,1}(undef, nn2)
ddd = Array{Float32,1}(undef, nn2)

## Computing d2a1 and d2d2a1
@inbounds for i=1:nn1
    @inbounds @simd for j=1:nn2
        d[j] = alpha[i,j,1] * conv2
    end
    deriv!( d, dd )
    deriv!( dd, ddd )
    @inbounds @simd for j=1:nn2
        jac[i,j,3] = dd[j]
        jac[i,j,7] = ddd[j]
    end
end

## Computing d2a2 and d2d2a2
@inbounds for i=1:nn1
    @inbounds @simd for j=1:nn2
        d[j] = alpha[i,j,2] * conv2
    end
    deriv!( d, dd )
    deriv!( dd, ddd )
    @inbounds @simd for j=1:nn2
        jac[i,j,4] = dd[j]
        jac[i,j,8] = ddd[j]
    end
end
```

```
## Computing mixed derivatives

## d2d1a1
@inbounds for i=1:nn1
    @inbounds @simd for j=1:nn2
        d[j] = jac[i,j,1] /conv1
    end
    deriv!( d, dd )
    @inbounds @simd for j=1:nn2
        jac[i,j,9] = dd[j]
    end
end
## d2d1a2
@inbounds for i=1:nn1
    @inbounds @simd for j=1:nn2
        d[j] = jac[i,j,2] /conv1
    end
    deriv!( d, dd )
    @inbounds @simd for j=1:nn2
        jac[i,j,10] = dd[j]
    end
end
## d1d2a1
@inbounds for j=1:nn2
    @inbounds @simd for i=1:nn1
        d[i] = jac[i,j,3] /conv2
    end
    deriv!( d, dd )
    @inbounds @simd for i=1:nn1
        jac[i,j,11] = dd[j]
    end
end
## d1d2a2
@inbounds for j=1:nn2
    @inbounds @simd for i=1:nn1
        d[i] = jac[i,j,4] /conv2
    end
    deriv!( d, dd )
    @inbounds @simd for i=1:nn1
        jac[i,j,12] = dd[j]
    end
end
```

```

        return jac
    end

function jac2kappa( jac::Array{Float32,3} )
    nn = size(jac)
    res = Array{Float32,2}( undef, nn[1], nn[2] )
    @inbounds for j=1:nn[2]
        @inbounds @simd for i=1:nn[1]
            res[i,j] = 0.5f0*( jac[i,j,1] + jac[i,j,4] )
        end
    end
    return res
end
#####
function jac2gamma1( jac::Array{Float32,3} )
    nn = size(jac)
    res = Array{Float32,2}( undef, nn[1], nn[2] )
    @inbounds for j=1:nn[2]
        @inbounds @simd for i=1:nn[1]
            res[i,j] = 0.5f0*( jac[i,j,1] - jac[i,j,4] )
        end
    end
    return res
end
#####
function jac2gamma2( jac::Array{Float32,3} )
    nn = size(jac)
    res = Array{Float32,2}( undef, nn[1], nn[2] )
    @inbounds for j=1:nn[2]
        @inbounds @simd for i=1:nn[1]
            res[i,j] = 0.5f0*( jac[i,j,2] + jac[i,j,3] )
        end
    end
    return res
end
#####
function jac2F1( jac::Array{Float32,3} )
    nn = size(jac)
    res = Array{Float32,2}( undef, nn[1], nn[2] )
    @inbounds for j=1:nn[2]
        @inbounds @simd for i=1:nn[1]
            res[i,j] = 0.5f0*(jac[i,j,5]-jac[i,j,12])
                + 0.5f0*(jac[i,j,7]+jac[i,j,10])
        end
    end
    return res
end

```

```

        end
    end
    return res
end
#####
function jac2F2( jac::Array{Float32,3} )
    nn = size(jac)
    res = Array{Float32,2}( undef, nn[1], nn[2] )
    @inbounds for j=1:nn[2]
        @inbounds @simd for i=1:nn[1]
            res[i,j] = 0.5f0*(jac[i,j,6]+jac[i,j,11])
                - 0.5f0*(jac[i,j,9]-jac[i,j,8])
        end
    end
    return res
end
#####
function jac2G1( jac::Array{Float32,3} )
    nn = size(jac)
    res = Array{Float32,2}( undef, nn[1], nn[2] )
    @inbounds for j=1:nn[2]
        @inbounds @simd for i=1:nn[1]
            res[i,j] = 0.5f0*(jac[i,j,5]-jac[i,j,12])
                -0.5f0*(jac[i,j,10]+jac[i,j,7])
        end
    end
    return res
end
#####
function jac2G2( jac::Array{Float32,3} )
    nn = size(jac)
    res = Array{Float32,2}( undef, nn[1], nn[2] )
    @inbounds for j=1:nn[2]
        @inbounds @simd for i=1:nn[1]
            res[i,j] = 0.5f0*(jac[i,j,6]+jac[i,j,11])
                + 0.5f0*(jac[i,j,9]-jac[i,j,8])
        end
    end
    return res
end
#####
function jac2rot( jac::Array{Float32,3} )
    nn = size(jac)

```

```

res = Array{Float32,2}( undef, nn[1], nn[2] )
@inbounds for j=1:nn[2]
    @inbounds @simd for i=1:nn[1]
        res[i,j] = 0.5f0*( jac[i,j,2] - jac[i,j,3] )
    end
end
return res
end
#####
function jac2crossderivativea1( jac::Array{Float32,3} )
    nn = size(jac)
    res = Array{Float32,2}(undef, nn[1], nn[2] )
    @inbounds for j=1:nn[2]
        @inbounds @simd for i=1:nn[1]
            res[i,j] = 0.5f0*(jac[i,j,11]-jac[i,j,9])
        end
    end
    return res
end
#####
function jac2crossderivativea2( jac::Array{Float32,3} )
    nn = size(jac)
    res = Array{Float32,2}(undef, nn[1], nn[2] )
    @inbounds for j=1:nn[2]
        @inbounds @simd for i=1:nn[1]
            res[i,j] = 0.5f0*(jac[i,j,10]-jac[i,j,12])
        end
    end
    return res
end

```

B Julia code for computing the galaxy-galaxy lensing correlation function

```

function winc( i::Int64, j::Int64, flexf1::Array{Float32,2},
flexf2::Array{Float32,2}, flexg1::Array{Float32,2}, flexg2::Array{Float32,2},
g1::Array{Float32,2}, g2::Array{Float32,2}, kappa::Array{Float32,2},
bb, cd2, acd1, rmin2, lrmin, dlr, nr, w::Vector{Float32}, ir::Vector{Int64},
kp::Vector{Bool} )

w[1] = (j-bb[6])*cd2 #y
w[2] = w[1]^2 #y2

```

```

w[3] = (i-bb[5])*acd1 #x
w[4] = w[3]^2 #x2
w[5] = w[4] + w[2] #r2
r = sqrt(w[5])
r3 = r^3
x3 = w[3]^3
y3 = w[1]^3
kp[1] = w[5]>rmin2
kp[1] || return
w[6] = ( -(w[4]-w[2])*g1[i,j] - 2.f0*w[1]*w[3]*g2[i,j] ) / w[5]
w[7] = kappa[i,j]
w[8] = (-flexf1[i,j]*w[3]-w[1]*flexf2[i,j])/r #-Re(F)
#w[8] = (flexf1[i,j]*w[1]-w[3]*flexf2[i,j])/r #-Im(F)
w[9] = -flexg1[i,j]*(4*(x3/r3)-3*w[3]/r)-flexg2[i,j]*(-4*(y3/r3)+3*w[1]/r)
#-Re(G)
#w[9] = -flexg2[i,j]*(4*(x3/r3)-3*w[3]/r)+flexg1[i,j]*(-4*(y3/r3)+3*w[1]/r)
#-Im(G)
ir[1] = ceil( Int64, (0.5f0*log(w[5])-lrmin)/dlr )
kp[1] = (ir[1]>=1) & (ir[1]<=nr)
end

#####
function comp_gs_corr( ra, dec, fn::AbstractString; rf=4,
dx=1.0f0, rmin=0.05f0, rmax=5f0, nr=50 )

ng=length(ra)
@assert length(dec)==ng

##### Deflection and derived information
@time (alpha,zz) = read_bin( fn )
nn=size(alpha)
@info "done reading deflection map!"
#@time jac=alpha2jac( alpha, scale=dx )
#@info "done computing 1st order derivatives!"
#@time jac=jac2der(jac)
@time jac = alpha2jac	flexion_w_cross_terms(alpha,scale=dx)
alpha=nothing ; GC.gc(true)
@info "done computing jacobian matrix map"
@time begin
    kappa = jac2kappa(jac)
    gamma1 = jac2gamma1(jac)
    gamma2 = jac2gamma2(jac)

```

```

F1 = jac2F1(jac)
F2 = jac2F2(jac)
G1 = jac2G1(jac)
G2 = jac2G2(jac)
end
jac=nothing ; GC.gc(true)
@info "done computing raw convergence, shear and flexion maps"
nn=(nn[1]/rf, nn[2]/rf)
@time begin
    kappa=rebin(kappa,factor=rf)
    gamma1=rebin(gamma1,factor=rf)
    gamma2=rebin(gamma2,factor=rf)
    F1=rebin(F1,factor=rf)
    F2=rebin(F2,factor=rf)
    G1=rebin(G1,factor=rf)
    G2=rebin(G2,factor=rf)
end
@info "done computing rebinned convergence & shear maps"
cd1 = -dx/nn[1] ; acd1=abs(cd1)
cr1 = (nn[1]+1)/2f0
cd2 = dx/nn[2]
cr2 = (nn[2]+1)/2f0

##### Rad bins
lrmin=log(rmin/60.f0) ; lrmax=log(rmax/60.f0) ;rmin2=(rmin/60.f0)^2
dlr=(lrmax-lrmin)/(nr)
W=ceil(Int64,rmax/abs(cd2)/60.f0)
rbin = exp.( range( lrmin, stop=lrmax, length=nr+1 ) ) ;

Sres=zeros(5,nr,ng)

#####
Threads.@threads for ig in eachindex(ra)
    bb=get_bbox2( ra[ig], dec[ig], W, cr1, cr2, cd1, cd2, nn )
    #afficher bb 1,2,3,4
    w=zeros(Float32,9)
    lres=zeros(Float64,5,nr)
    ir=[1]
    kp=[false]

    @inbounds for j=bb[3]:bb[4]
        @inbounds for i=bb[1]:bb[2]
            winc( i, j, F1, F2, G1, G2, gamma1, gamma2, kappa,

```

```
bb, cd2, acd1, rmin2, lrmin, dlr, nr, w, ir, kp )
if kp[1]
    lres[1,ir[1]] += Float64(w[9]) #storing G+
    lres[2,ir[1]] += Float64(w[8]) #storing F+
    lres[3,ir[1]] += Float64(w[7]) #storing kappa
    lres[4,ir[1]] += Float64(w[6]) #storing gamma+
    lres[5,ir[1]] += 1.0           #counting pixels
end
end
Sres[:, :, ig] .= lres
end
# Sres = pmap( ig->loc_calc(ra[ig],dec[ig]), 1:ng )
# res = sdata(Sres)
return Sres, rbin, kappa
end
```

List of Figures

2.1	Definition of lensing angles and distances. Figure by Michael SACHS	5
2.2	Effects of the different lensing fields on a Gaussian galaxy of radius 1 arcsec. 10% convergence/shear and 0.28 arcsec^{-1} flexion (which is a very large value for this quantity, chosen only for visualizing) are applied. Figure extracted from [2]	7
3.1	Two dimensional graph of the past lightcone generated with Horizon-AGN. Each blue cell is a replicate of the H-AGN simulation box. The orange vertical line marks $z = 1$ and the tiling repeats up to $z = 8$. The black lines represents the aperture angle of the cone which goes from 2.25 arcseconds to 1.00 arcsec- ond after $z = 1$. Figure extracted from [6]	9
3.2	Expressions as derivatives of the two components of the deflection fields of the seven lensing quantities defined earlier and used	11
3.3	Tangential projection of the lensing quantities, generated by gravitational lensing, used to effectively compute and measure the lensing quantities.	12
3.4	Cross projection of the lensing quantities, which should yield no signal and thus can be used as a robust way of checking for systematical errors.	12
3.5	Tangential projection of the lensing quantities, expressed in flat sky plane coordinate.	12
3.6	Cross projection of the lensing quantities, expressed in flat sky plane coordinates.	13
3.7	The process of measuring the galaxy-galaxy lensing correlation statistic. Fig- ure by Masamune Oguri	18
4.1	Convergence map for a redshift $z_{plane} \approx 1.016$, computed from a combination of derivatives of the two deflection field maps.	21
4.2	The two different shear fields γ_1 and γ_2	21
4.3	The four different flexion fields $\mathcal{F}_1, \mathcal{F}_2$ and $\mathcal{G}_1, \mathcal{G}_2$. Computed by the code in Appendix A.	22
4.4	Galaxy-Galaxy lensing correlations for each component and arbitrary lens planes	23
4.5	Galaxy-Galaxy lensing correlations for each component and arbitrary lens planes	25
4.6	Lensing signals for each component, fitted with the SIS and NFW models. Computed by the code in Appendix B.	26
4.7	Lensing signals for each component, fitted with the SIS and NFW models. Computed by the code in Appendix B.	27

List of Tables

3.1	List of parameters used for the flat Λ CDM cosmology defined in the Horizon-AGN simulation and their values, all parameters are unitless, except for the Hubble parameter H_0 , expressed in $\text{km s}^{-1}\text{Mpc}^{-1}$	8
3.2	Available information in the header of the galaxy catalog within the Horizon-AGN simulated light cone.	16

List of Listings
